

1 Thank you for your careful reading of the manuscript. The suggested technical corrections
2 have been made and the point-by-point responses are listed below in blue font.

3

4 1) line 311: “above” should be “below”

5 Text changed as suggested.

6

7 2) line 314: “(by multiplying the activation tendency in equation (1) by 0.5)” as well as
8 the justification of this ad-hoc assumption has been deleted, but I think this detail is
9 important and should be kept in the manuscript.

10 These details have been added back to the paragraph and the text now reads, “After
11 the initial time 50% of the IN available in a bin nucleates if the in-situ temperature is
12 below the threshold temperature and the local conditions exceed water saturation.

13 Therefore, initial N_{IN} concentrations are a function of the nucleation threshold
14 temperatures and are independent of the in-situ temperature. The in-situ temperature
15 in regions of water saturation determines how many IN are activated. The activation
16 of 50% of the available IN is used to take deviations from the empirical derivation
17 into account, however results are insensitive to this parameter (not shown).”

18

19 3) line 337: insert “of” before “the coldest bin”

20 Text changed as suggested.

21

22 4) Also at line 337, you should give here the information provided in the replies, namely
23 that -20.2°C is the coldest temperature reached in the reference run.

24 This sentence has been rewritten to read, “Using a discrete bin formulation to
25 represent eq. (2) and assigning the coldest bin to the coldest temperature reached by
26 the Control simulation (-20.2°C) results in 3.26 L⁻¹ in the warmest bin and 0.23 L⁻¹
27 additional IN that are available for nucleation in the coldest bin.”

28

29 5) I actually suggest to add “at -20.2°C” after “5.8 L⁻¹” in line 334, because IN
30 concentrations should always be given together with the conditions which they refer

31 to. (If you had chosen to extend the temperature bins down to e.g. -22°C , this value
32 would have been different.)
33 [Sentence changed as suggested.](#)

34 The Role of Ice Nuclei Recycling in the Maintenance of Cloud Ice in

35 Arctic Mixed-Phase Stratocumulus

36 Amy Solomon¹², Graham Feingold², and Matthew D. Shupe¹²

37 (1) Cooperative Institute for Research in Environmental Sciences, University of Colorado

38 Boulder, Boulder, Colorado, USA.

39 (2) Earth System Research Laboratory, National Oceanic and Atmospheric Administration,

40 Boulder, Colorado, USA.

41

42 Corresponding author: Amy Solomon, NOAA/ESRL, PSD3, 325 Broadway, Boulder,

43 Colorado 80305-3337, USA. (amy.solomon@noaa.gov)

44 September 14, 2015

46 This study investigates the maintenance of cloud ice production in Arctic mixed phase
47 stratocumulus in large eddy simulations that include a prognostic ice nuclei (IN) formulation
48 and a diurnal cycle. Balances derived from a mixed-layer model and phase analyses are used
49 to provide insight into buffering mechanisms that maintain ice in these cloud systems. We
50 find that for the case under investigation, IN recycling through subcloud sublimation
51 considerably prolongs ice production over a multi-day integration. This effective source of
52 IN to the cloud dominates over mixing sources from above or below the cloud-driven mixed
53 layer. Competing feedbacks between dynamical mixing and recycling are found to slow the
54 rate of ice lost from the mixed layer when a diurnal cycle is simulated. The results of this
55 study have important implications for maintaining phase partitioning of cloud ice and liquid
56 that determine the radiative forcing of Arctic mixed-phase clouds.

57 **1 Introduction**

58 Reliable climate projections require realistic simulations of Arctic cloud feedbacks. Of
59 particular importance is accurately simulating Arctic mixed-phase stratocumuli (AMPS),
60 which are ubiquitous and play an important role in regional climate due to their impact on the
61 surface energy budget and atmospheric boundary layer structure through cloud-driven
62 turbulence, radiative forcing, and precipitation (Curry et al., 1992; Walsh and Chapman,
63 1998; Intrieri et al., 2002; Shupe and Intrieri, 2004; Sedlar et al., 2011; Persson, 2012). For
64 example, Bennartz et al. (2012) showed that the extreme melt events observed at Summit,
65 Greenland in July 2012 would not have occurred without the surface radiative forcing
66 produced by AMPS.

67 AMPS are characterized by a liquid cloud layer with ice crystals that precipitate from cloud
68 base even at temperatures well below freezing (Hobbs and Rangno, 1998; Intrieri et al.,
69 2002; McFarquhar et al., 2007). Radiative cooling near cloud top generates turbulence that
70 maintains the liquid layer and forms an approximately well-mixed layer that extends as far as
71 500 meters below cloud base. These cloud-driven mixed layers are frequently decoupled
72 from the surface layer, limiting the impact of fluxes of heat, moisture, and aerosols on the
73 cloud layer from below (Solomon et al., 2011; Shupe et al., 2013). However, unlike
74 subtropical cloud-topped boundary layers where decoupling enhances cloud breakup by
75 cutting the cloud system off from the surface source of moisture, decoupled AMPS can
76 persist for extended periods of time due to weak precipitation fluxes out of the mixed layer
77 and relatively moist air entrained into the cloud layer at cloud top (Tjernström et al., 2004;
78 Solomon et al., 2011; Sedlar et al., 2012; Solomon et al., 2014).

79 AMPS are challenging to model due to uncertainties in ice microphysical processes that
80 determine phase partitioning between ice and radiatively important cloud liquid water
81 (Sandvik et al., 2007; Tjernström et al., 2008; Klein et al., 2009, Karlsson and Svensson,
82 2011; Barton et al., 2012; Birch et al., 2012; de Boer et al., 2012), which drives turbulence
83 that maintains the system. Phase partitioning depends upon the number, shape, and size of ice
84 crystals, since these determine the efficiency of water vapor uptake by ice and hence the
85 availability of water vapor for droplet formation (Chen and Lamb, 1994; Sheridan et al.,
86 2009; Ervens et al., 2011; Hoose and Möhler, 2012).

87 Since temperatures in AMPS are too warm for homogenous ice nucleation, ice must form
88 through heterogeneous nucleation. Aerosols with properties to serve as seeds for
89 heterogeneous ice crystal formation are referred to as ice nuclei (IN). A number of different
90 aerosols such as mineral dust (Broadley et al., 2012; Kulkarni et al., 2012; Lüönd et al., 2010;
91 Möhler et al. 2006; Pinti et al., 2012; Welte et al., 2009), soot (DeMott, 1990), sea salts (Wise
92 et al., 2012), and bacteria (Kanji et al., 2011; Levin and Yankofsky, 1983) have been
93 observed to act as IN, all of which nucleate at different temperatures and supersaturation
94 ranges. In addition, observations indicate that nucleation properties are modified by aging
95 and coating of aerosols (Möhler et al., 2005; Cziczo et al. 2009). Heterogeneous ice
96 nucleation can occur by a number of modes: either in the presence of super-cooled droplets,
97 when an aerosol comes into contact with a droplet (contact freezing), is immersed in a
98 droplet (immersion freezing), or by vapor deposition on IN (deposition freezing) (Pruppacher
99 and Klett, 1997).

100 IN can be entrained into the cloud-driven mixed layer through turbulent mixing from above
101 and/or below. Recent studies indicate that entrainment alone cannot account for observed ice
102 crystal number concentration (N_{ICE}) (Fridlind et al., 2012), motivating the use of diagnostic
103 formulations for ice formation to produce model simulations of AMPS with realistic phase
104 partitioning (Ovchinnikov et al., 2011). While this modeling strategy constrains N_{ICE} to be
105 close to the measured values it eliminates the dynamical-microphysical feedbacks that
106 regulate ice/liquid phase partitioning (Avramov et al., 2011).

107 Here we investigate a relatively unexplored source of ice production--recycling of ice nuclei
108 in regions of ice subsaturation. AMPS frequently have ice-subsaturated air near the cloud-
109 driven mixed-layer base where falling ice crystals can sublimate, leaving behind IN. This
110 feedback loop is referred to hereon as “recycling”. Recycling was found to be significant in
111 large eddy simulations of a single-layer stratocumulus observed during the Department of
112 Energy Atmospheric Radiation Measurement Program’s Mixed-Phase Arctic Cloud
113 Experiment (M-PACE; Verlinde et al., 2007; Fan et al., 2009). AMPS observed during M-
114 PACE formed due to a cold-air outbreak, where large fluxes of heat and moisture over the
115 open ocean forced turbulent roll clouds that were coupled to the surface layer. This coupling
116 with the surface layer prevented the identification of the role of dynamics internal to the
117 cloud-driven mixed layer in maintaining phase-partitioning.

118 In this study we focus on the internal microphysics and dynamics of the cloud-driven mixed
119 layer by investigating processes in an AMPS decoupled from surface sources of moisture,
120 heat, and ice nuclei. We posit that recycling plays a significant role more generally since, for
121 example, assuming an adiabatic vertical profile, a 650 meter-deep mixed layer with a cloud-

122 top temperature of -16°C requires a water vapor mixing ratio of at least 1.7 g kg^{-1} at mixed-
123 layer base to be saturated with respect to ice, i.e., in order for recycling to be a *negligible*
124 source of ice nuclei in the mixed layer. This value is typically only seen in the Arctic
125 between May-September (Serreze et al., 2012), while persistent AMPS frequently occur
126 outside of these months (Shupe et al., 2011).

127 We examine the role of IN recycling in maintaining ice production using large eddy
128 simulations of a springtime decoupled AMPS. Three simulations are analyzed; a “Control”
129 with recycling turned on and shortwave radiation turned off (to compare with previous
130 simulations of this case that use different IN formulations and shortwave radiation turned off),
131 “NoRecycle” with IN recycling turned off to identify the impact of recycling on the cloud
132 life-time and phase partitioning, and “SW” with recycling and shortwave radiation turned on
133 to identify the impact of realistic diurnal heating and cooling tendencies on the recycling
134 process. This study builds on previous studies of this case, all of which exclude shortwave
135 radiation (Avramov et al., 2011; Solomon et al., 2011, 2014), by including a prognostic
136 equation for IN and a diurnal cycle. Within this modeling framework we investigate the
137 relative roles of recycling and entrainment of IN in maintaining cloud ice production.

138 **2 Case Description**

139 The case derives from observations of a persistent single-layer Arctic mixed-phase
140 stratocumulus cloud observed near Barrow, AK on 8 April 2008 during the Indirect and
141 Semi-Direct Aerosol Campaign (McFarquhar et al., 2011) (see Fig. 1). The adjacent Beaufort
142 Sea was generally ice covered during this time, with significant areas of open water observed
143 east of Barrow. A 4-K temperature inversion with inversion base at 1.05 km was observed

144 via a radiosonde at 17:34UTC; static stability was near neutral within the mixed layer
145 overlaying a stable near-surface layer with static stability greater than 2 K km^{-1} below 500 m.
146 The water vapor mixing ratio, q_v , decreased from 1.7 g kg^{-1} at the surface to 1.2 g kg^{-1} at
147 cloud top, above which a secondary maximum of 1.6 g kg^{-1} was observed. Winds were east-
148 southeasterly throughout the lowest 2 km.

149 Measurements from ground-based, vertically pointing, 35-GHz cloud radar, micropulse lidar,
150 and dual-channel microwave radiometer at Barrow indicated a mixed-phase cloud layer
151 starting at 8 UTC on 8 April 2008 with a cloud top at approximately 1.5km that slowly
152 descended to approximately 0.5 km over a 26 hour period. At the time of the 17:34 sounding
153 the cloud layer extended into the inversion by 100 m, had a cloud base at 0.9 km, and cloud
154 top at 1.15 km. Cloud ice water path (IWP), derived from cloud radar reflectivity
155 measurements, varied from $20\text{--}120 \text{ g m}^{-2}$ within 10 min of the sounding, with an uncertainty
156 of up to a factor of 2 (Shupe et al., 2006). Concurrently liquid water path (LWP), derived
157 from dual-channel microwave radiometer measurements, was $39\text{--}62 \text{ g m}^{-2}$, with an
158 uncertainty of $20\text{--}30 \text{ g m}^{-2}$ (Turner et al., 2007).

159 Research flights were conducted by the National Research Council of Canada Convair-580 at
160 22:27-23:00 UTC on 8 April 2008 over the ocean northwest of Barrow (McFarquhar et al.,
161 2011). Droplet concentrations measured by a Particle Measuring Systems Forward Scattering
162 Spectrometer Probe varied between 100 and 200 cm^{-3} . Ice crystal number concentrations
163 measured by Stratton Park Engineering Company 2D-S and Particle Measuring Systems 2D-
164 P optical array probes for sizes larger than 100 μm together averaged 0.4 L^{-1} . IN
165 concentrations measured with the Texas A&M Continuous Flow Diffusion Chamber varied

166 from 0.1 L^{-1} to above 20 L^{-1} . Ice crystal habit estimated using the automated habit
167 classification procedure of Korolev and Sussman (2000) indicated primarily dendritic crystal
168 habits.

169 **3 Model Description**

170 We use the large eddy simulation mode of the Advanced Research WRF model (WRFLES)
171 Version 3.3.1 (Yamaguchi and Feingold, 2012) with the National Center for Atmospheric
172 Research Community Atmospheric Model longwave radiation package (Collins et al., 2004),
173 RRTMG shortwave package (Iacono et al., 2008), the Morrison two-moment microphysical
174 scheme (Morrison et al., 2009), and a 1.5-order turbulent kinetic energy prediction scheme
175 (Skamarock et al., 2008). Surface fluxes are calculated uses the modified MM5 similarity
176 scheme which calculates surface exchange coefficients for heat, moisture, and momentum
177 following Webb (1970) and uses Monin-Obukhov with Carlson-Boland viscous sub-layer
178 and standard similarity functions following Paulson (1970) and Dyer and Hicks (1970).

179 All model runs are initialized with winds, temperature, and water vapor from the 17Z 8 April
180 2008 sounding at Barrow, AK (see Fig.1). Initial surface pressure is 1020 hPa. Divergence is
181 assumed to be $2.5 \times 10^{-6} \text{ s}^{-1}$ below the temperature inversion and zero above, giving a linear
182 increase in large-scale subsidence from zero at the surface to 2.7 mm s^{-1} at the base of the
183 initial inversion ($z=1.1 \text{ km}$). This value for divergence was chosen so that the height of the
184 temperature inversion at cloud top is steady. The divergence used in this study is smaller than
185 the divergence used in the WRFLES study of the same case by Solomon et al. (2014) due to

186 the reduced LWPs in this current study and therefore reduced turbulent entrainment that
187 balances large-scale subsidence in a steady simulation.

188 All simulations are run on a domain of $3.2 \times 3.2 \times 1.8$ km with a horizontal grid spacing of
189 50 m and vertical spacing of 10 m. The domain has $65(x) \times 65(y) \times 180(z)$ gridpoints and is
190 periodic in both the x- and y-directions. The top of the domain is at 1.8 km, which is 0.7 km
191 above cloud top in this case. The model time step is 0.75 s. The structure of the cloud layer is
192 insensitive to changes in resolution and domain size. For example, tests run for Solomon et al.
193 (2014) demonstrated that increasing the vertical and horizontal resolutions by a factor of two
194 resulted in an increase in LWP and IWP by 5% and 1%, respectively, while increasing the
195 domain size by a factor of two in both the x- and y-directions results in an increase in LWP
196 and IWP of less than 1%.

197 Cloud droplets are activated using resolved and subgrid vertical motion (Morrison and Pinto
198 2005) and a log-normal aerosol size distribution (assumed to be ammonium bisulfate and
199 30% insoluble by volume) to derive cloud condensation nuclei spectra following Abdul-
200 Razzak and Ghan (2000). The aerosol accumulation mode is specified with concentrations of
201 165 cm^{-3} , modal diameter of $0.2 \mu\text{m}$, and geometric standard deviation of 1.4, based on
202 in situ ISDAC measurements. In this formulation, IN and cloud condensation nuclei are
203 treated as separate species.

204 Temperature and moisture profiles are nudged to the initial profiles in the top 400 m of the
205 domain with a time scale of 1 hour. The model is initialized with winds, temperature, and
206 water vapor similar to the Control integration from Solomon et al. (2014). Horizontal winds
207 are nudged to the initial profiles at and above the initial inversion base with a timescale of 2

208 hours. Initial temperature and subgrid turbulent kinetic energy (TKE) are perturbed below the
209 top of the mixed layer with pseudo-random fluctuations with amplitudes of +/- 0.1 K and 0.1
210 $\text{m}^2 \text{s}^{-2}$, respectively. The liquid layer is allowed to form in the absence of ice during the first
211 hour of the integration to prevent potential glaciation during spinup.

212 The cloud-driven mixed layer is defined as the region where the liquid-ice water static energy
213 is approximately constant with height. We define the boundaries of the mixed-layer top and
214 base to occur where the slopes of liquid-ice static energy exceed $7 \times 10^{-3} \text{ K m}^{-1}$ and $1 \times 10^{-3} \text{ K}$
215 m^{-1} , respectively. Cloud top and base are defined as the heights where cloud water mixing
216 ratio, q_c , is equal to $1 \times 10^{-4} \text{ g kg}^{-1}$.

217 Nested Weather Research and Forecasting (WRF) model simulations of this case performed
218 with an inner grid at LES resolution (Solomon et al. 2011) demonstrate that moisture is
219 provided to the cloud system by a total water inversion at cloud top and that the mixed layer
220 does not extend to the surface, i.e., the mixed layer is largely decoupled from surface sources
221 of moisture. In addition, the nested simulations indicate that cloud liquid water, q_c , is
222 maintained within the temperature inversion by downgradient turbulent fluxes of q_v from
223 above and direct condensation driven by radiative cooling. These processes cause at least
224 20% of q_c to extend into the temperature inversion.

225 WRFLES has been modified to include a prognostic equation for IN number concentration
226 (N_{IN}),

$$\frac{\partial N_{IN}}{\partial t} + ADV + DIFF = \left. \frac{\delta N_{IN}}{\delta t} \right|_{activation} + \left. \frac{\delta N_{IN}}{\delta t} \right|_{sublimation} \quad (1)$$

227 where ADV represents advection and DIFF represents turbulent diffusion. Activation is also
228 referred to as nucleation of ice and sublimation is also referred to as recycling of IN.

229 Here we adopt an empirical approach by initializing N_{IN} with an observationally based
230 relationship expressing the number of available IN as a function of temperature in regions of
231 water-saturation (DeMott et al., 2010),

$$N_{IN} = F * 0.117 \exp(-0.125 * (T - 273.2)) \quad (2)$$

232 where F is an empirically derived scale factor and T is temperature in Kelvin. Sixteen
233 prognostic equations are integrated for N_{IN} in equally spaced temperature intervals with
234 nucleation thresholds between -20.2°C and -15.5°C (see Fig. 2). Therefore, additional IN
235 become available for activation with decreasing temperature and as the cloud layer cools. IN
236 number concentrations are initially specified using equation 2, such that the initial IN in bin k
237 is equal to the number of IN calculated by equation 2 at the threshold temperature $k + 1$
238 minus that calculated at temperature k . After the initial time 50% of the IN available in a bin
239 nucleates if the in-situ temperature is below the threshold temperature and the local
240 conditions exceed water saturation. Therefore, initial N_{IN} concentrations are a function of the
241 nucleation threshold temperatures and are independent of the in-situ temperature. The in-situ
242 temperature in regions of water saturation determines how many IN are activated. The
243 activation of 50% of the available IN is used to take deviations from the empirical derivation
244 into account, however results are insensitive to this parameter (not shown). Due to the
245 pristine dendritic nature of the observed crystals, ice shattering and aggregation are neglected
246 in the simulations and sublimation returns one N_{IN} per crystal.

Amy Solomon NOAA 9/14/2015 9:55 AM

Deleted: above

248 N_{IN} (in units of L^{-1}) integrated over the domain in each temperature bin k at time t is equal to

$$\bar{N}_{IN}(k, t) = \iiint N_{IN}(x, y, z, k, t) dx dy dz. \quad (3)$$

249 Upon sublimation, the modification of activation thresholds that can occur for previously
250 nucleated IN, i.e. preactivation (Roberts and Hallett, 1967), is not considered and N_{IN} are
251 returned to each bin k with weighting

$$W_k = [\bar{N}_{IN}(k, 0) - \bar{N}_{IN}(k, t)] / \bar{N}_{IN}(k, 0) \quad (4)$$

252 where W_k is normalized such that $\sum W_k = 1$. The W_k are recalculated each time step. In this
253 way, IN are recycled preferentially to each of the 16 temperature bins from which they
254 originated (Feingold et al., 1996).

255 The factor F in Eq. (2) is set to 4 for all simulations yielding an initial N_{IN} summed over all
256 bins at every gridpoint equal to $5.8 L^{-1}$ at $20.2^\circ C$, compared to $10 L^{-1}$ used in LES studies of
257 the same case presented in Avramov et al. (2011). Using a discrete bin formulation to
258 represent eq. (2) and assigning the coldest bin to the coldest temperature reached by the
259 Control simulation ($-20.2^\circ C$), results in $3.26 L^{-1}$ in the warmest bin and $0.23 L^{-1}$ additional IN
260 that are available for nucleation in the coldest bin. Given the initial temperatures in the cloud
261 layer, all IN from the first bin in the cloud layer nucleate. This causes an initial spike in cloud
262 ice number concentration, which also causes a large precipitation flux out of the mixed layer.
263 It takes approximately 6 hours for the cloud layer to reach a quasi-equilibrium with steady
264 cloud ice production. Supplementary integrations were done to test for robustness of the
265 results presented in Section 4 by varying initial IN concentrations, i.e., the factor F , (shown

Amy Solomon NOAA 9/14/2015 2:32 PM

Deleted: ,

Amy Solomon NOAA 9/14/2015 2:29 PM

Deleted: In a

Amy Solomon NOAA 9/14/2015 2:30 PM

Deleted: this

Amy Solomon NOAA 9/14/2015 2:26 PM

Deleted: , resulting in N_{IN} given by eq. (2) evaluated at the temperature the coldest bin ($-20.2^\circ C$).

272 in Fig. 3) and by varying snow density and fall speeds (shown in Fig. 4). Fig. 3 shows that
273 the simulation maintains ice production when the initial N_{IN} is increased or decreased by ~ 3
274 L^{-1} relative to Control. Fig. 4 shows that the simulations maintain quasi-steady ice and liquid
275 water paths after an initial spinup but the amount of ice produced is sensitive to the snow fall
276 speed.

277 Crystal size distributions for averaged values of ice water mixing ratio and number
278 concentration from the Control integration are shown in Fig. 5. These crystal size
279 distributions are consistent with the Avramov et al. (2011) simulations of this case where
280 crystal habits are assumed to be high-density pristine dendrites. The distribution shown in Fig.
281 5 underestimates the number of large (greater than 5mm) crystals as estimated by the 2D-S
282 and 2D-P probes (see Avramov et al. (2011) for a detailed discussion of the measurements).

283 The Control integration is run with shortwave radiation turned off in order to compare with
284 previous LES studies of this case (Avramov et al. 2011; Solomon et al. 2014). The results of
285 Control are compared to two additional simulations; one with IN recycling turned off
286 (hereafter “NoRecycle”) and one with recycling and shortwave radiation both turned on
287 (hereafter “SW”). SW is used to investigate how the diurnal cycle impacts IN recycling and
288 ice formation. All runs use the same setup except SW has subsidence reduced by 30% to
289 keep the mixed-layer top from lowering appreciably because of smaller LWPs. This allows
290 for direct comparisons of mixed layer structure and fluxes at the mixed layer boundaries. The
291 NoRecycle run is started from the Control run at hour 6 to prevent the two simulations from
292 diverging due to spinup. The first six hours of integration are not used in the analysis to allow
293 for the spinup of cloud ice. Hours 6-40 are used for analysis of the Control and NoRecycle

294 simulations and hours 16-76 are used for analysis of the SW simulation to allow for multiple
295 diurnal cycles.

296 **4 Model Results**

297 **4.1 Control Integration**

298 In the quasi-steady Control integration, the mixed-layer depth is approximately 850 m and
299 comprises a 375 m deep mixed-phase cloud layer (henceforth “the cloud layer”), extending
300 above the mixed-layer top by 25 m, and a 500 m subcloud layer below (Fig. 6). IN are
301 produced by sublimation of ice crystals below the cloud layer, advected to the cloud layer by
302 turbulence, and activated as ice crystals (Fig. 6). Ice that forms in the cloud layer is
303 transported vertically by turbulence, precipitates to cloud base and below, and sublimates
304 below the cloud layer. At the mixed-layer base, an increase in N_{ICE} due to precipitation
305 approximately balances a decrease in N_{ICE} due to sublimation. These processes constitute a
306 feedback through which ice production and IN recycling are closely related. This feedback
307 between ice production and IN in the mixed layer is linked to dynamic-thermodynamic
308 tendencies, which sustain a subsaturated subcloud layer because the decrease in relative
309 humidity due to an upward turbulent vapor flux exceeds the increase due to sublimation.

310 The time evolution of horizontally-averaged IN advection plus subsidence (Fig. 7a) shows
311 that the majority of IN activate at cloud base, which is a bit warmer than cloud top but is
312 sufficiently cold to activate many of the IN. However, IN from bins with colder threshold
313 temperatures are advected higher into the cloud where they activate at their threshold
314 temperature. A secondary maximum is seen at cloud top where the coldest temperatures are

315 found. Also, it is seen that IN are advected into the cloud layer at cloud top for the first 15-18
316 hours, but this source of IN decreases as IN in the upper entrainment zone are depleted. The
317 turbulent mixing of snow and ice in the mixed-phase cloud layer is clearly seen in Fig. 7b,
318 where ice plus snow number concentrations are well-mixed in the cloud layer. Given the
319 efficient mixing by the turbulent eddies, it is not possible to identify whether ice has
320 nucleated at cloud base or cloud top from the ice number concentrations alone. Fig. 7 also
321 shows the time-height cross sections of horizontally-averaged water vapor mixing ratio and
322 relative humidity with respect to ice. These figures show that the continuous drying and
323 cooling of the mixed layer results in continuous sublimation in the subcloud layer.

324 LWP and IWP remain steady until hour 16 of the simulation, and decrease slowly thereafter
325 (solid lines in Fig. 8a). LWP and IWP magnitudes are within the observational estimates for
326 this case. In addition, the cloud system is sustained over a multi-day period similar to
327 measurements taken during ISDAC. Continuous cloud-top cooling causes the minimum
328 horizontally-averaged temperature (near cloud top) to decrease from -17.5°C to -20°C from
329 hour 10 to hour 40 (Fig. 8b).

330 Over the 40-hour integration, the mixed layer remains decoupled from the surface (Fig. 8c).
331 However, this does not prevent the number concentration of ice crystals (N_{ICE}) in the cloud
332 layer from remaining relatively steady, decreasing from vertically integrated values of 372 to
333 365 m L^{-1} (Fig. 8d, or in terms of vertically averaged cloud layer values, 1.2 L^{-1} to 1.1 L^{-1}).
334 By contrast, while N_{ICE} is maintained in the cloud layer, N_{IN} in the subcloud layer decreases
335 significantly from 2 L^{-1} to 0.2 L^{-1} over the same period. Therefore, even though more N_{ICE}
336 are lost from the cloud than are activated (Fig. 9a), the relatively constant flux of IN into the

337 cloud layer (Fig. 9b) allows N_{ICE} in the cloud to decrease at a slower rate than N_{IN} in the
338 subcloud layer. The continuous loss of N_{IN} in the subcloud layer is due to the IN flux into the
339 cloud layer exceeding the N_{IN} gained through sublimation and turbulent advection at mixed-
340 layer base (Fig. 9b). This loss is not mitigated by entrainment at mixed-layer top, which is
341 found to be negligible (Fig. 9c), consistent with Fridlind et al. (2011).

342 The feedback loops discussed above are illustrated by the conceptual diagram in Fig. 10,
343 where any change to one link in the cycle leads to an increase or decrease in ice production.
344 For example, a decrease in the turbulent advection of N_{IN} into the cloud layer, slows the
345 activation of IN, reduces the precipitation flux into the subcloud layer, reducing sublimation
346 and availability of IN below cloud base. Both dynamics and thermodynamics play a role in
347 the buffering aspect of these feedback loops since, for example, the slowing of IN activation
348 in the example above would lead to increased cloud liquid production, cloud-top radiative
349 cooling, and enhanced turbulent mixing, which would lead to increased transport of IN into
350 the cloud layer and therefore increased activation of IN.

351 ***4.2 Impact of turning off recycling***

352 When IN recycling is turned off, all IN that activate are lost from the system. This results in a
353 more rapid loss of IN, a decrease in IWP, and a rapid increase in LWP (Fig. 8a,d, dashed
354 lines), in contrast to the measurements that show a steady liquid layer and consistent ice
355 production. Increased cloud liquid water when recycling is turned off results in increased
356 radiative cooling at cloud top, which causes the cloud-driven mixed layer to cool more
357 rapidly (Fig. 8b). These results demonstrate the importance of IN recycling in regulating

358 phase partitioning. The rapid increase in LWP increases cloud-generated turbulence via
359 enhanced radiative cooling and increases the turbulent mixing of IN from the subcloud layer
360 into the cloud layer, contributing to a more rapid depletion of IN relative to the Control
361 integration. This process eventually becomes limited due to depletion of IN in the reservoir
362 below (Fig. 9b). Due to the additional activation of IN as the cloud layer cools, ice
363 production is maintained in the absence of recycling and the activation of IN in the cloud
364 layer exceeds the upward IN flux at cloud base (Fig. 9a,b). However, the diminishing N_{IN} in
365 the subcloud layer limits IN activation and N_{ICE} rapidly decreases in the cloud layer (Fig. 8d).

366 ***4.3 Impact of diurnal cycle***

367 A diurnal cycle is added to the Control simulation in order to investigate how the feedback
368 loops identified in the Control and NoRecycle runs are modified with realistic transient
369 heating and cooling tendencies due to variations in incoming shortwave radiation. A question
370 that is addressed in this diurnal simulation is, to what extent is the continuous production of
371 ice in the Control simulation due to the lack of incoming shortwave radiation, which may
372 overestimate the cooling tendencies in the cloud layer, resulting in an overestimate of IN
373 activation? In addition, we investigate whether allowing for a realistic diurnal cycle provides
374 for additional negative or “buffering” feedbacks.

375 Adding a diurnal cycle to the Control simulation produces a diurnal peak in downwelling
376 surface shortwave radiation of 510 W m^{-2} and 6 hours of total darkness per day (Fig. 11b).
377 As shortwave radiation increases, the net radiative cooling near cloud top diminishes, which
378 decreases cloud-generated turbulence, decreasing LWP and cloud-layer thickness. In addition,

379 it is seen that the peak daily LWP coincides with zero shortwave radiation when in-cloud
380 turbulence and cloud thickness are largest (Fig. 11a). These values are on the low end but
381 within the measurements for this ISDAC case.

382 Fig. 11a,b shows that LWP and IWP variability is predominantly driven by the diurnal cycle.
383 However, IWP variability is seen to lag LWP by 3-4 hours because as shortwave radiation
384 decreases the cloud layer cools, which increases activation of IN, increasing N_{ICE} , allowing
385 more ice crystals to grow, which increases IWP (Fig. 11a,b). Similar to the Control
386 simulation subcloud N_{IN} decreases at a faster rate than cloud layer N_{ICE} , but allowing for the
387 warming and cooling tendencies in the diurnal cycle results in cloud layer N_{ICE} that decreases
388 40% more slowly than in the Control simulation (Fig. 11c).

389 Precipitation and turbulent mixing of N_{ICE} (hereafter turbulent mixing is referred to as
390 " T_{ICE} ") at cloud base are out of phase by 10 hours (Fig. 11d), with turbulence leading
391 precipitation. When shortwave radiation is weak or absent, the increase in N_{ICE} eventually
392 becomes limited by a decreasing turbulent mixing of IN (" T_{IN} ") into the cloud layer from
393 below, as recycling slows due to a decrease in N_{ICE} flux from the cloud layer (Fig. 11d,f).
394 When shortwave radiation is strong, reduction in IWP is limited by weaker precipitation
395 losses, and attendant weaker sublimation and IN flux into the cloud layer (Fig. 11d,f).
396 Entrainment of N_{IN} at the mixed-layer top is insignificant throughout the integration (Fig.
397 11e).

398 **5 Analysis from a mixed-layer perspective**

399 The results discussed in Section 4 can be understood from balances in a well-mixed layer
 400 with sources/sinks at the upper and lower boundaries. Total particle concentration
 401 ($N_{IN}+N_{ICE}$) is only changed by fluxes at the mixed-layer boundaries when recycling is
 402 allowed. These fluxes are entrainment of N_{IN} at mixed-layer top and turbulent mixing of both
 403 N_{ICE} and N_{IN} (T_{ICE} and T_{IN}) and precipitation of N_{ICE} (P) at mixed-layer base. Since there
 404 are no sources and sinks of $N_{IN}+N_{ICE}$ within the mixed layer, the horizontally-averaged
 405 $N_{IN}+N_{ICE}$ flux ($f(z)$) must vary linearly from mixed-layer base to mixed-layer top (Lilly,
 406 1968; Bretherton and Wyant, 1997). If it is assumed that f at the mixed-layer base is
 407 downward (assumed negative in this formulation) and f at the mixed-layer top is negligible
 408 (robust assumptions for a scenario where ice is precipitating from the mixed layer and
 409 entrainment is weak), then

$$f(z) = R * \frac{H - z}{H - B}, \quad B \leq z \leq H \quad (5)$$

410 where H is the mixed-layer height, B is the mixed-layer base and R is the total $N_{IN}+N_{ICE}$ flux
 411 at the mixed-layer base,

$$R = f|_{\text{Mixed-Layer Base}} = [P + T_{ICE} + T_{IN}]_{\text{Mixed-Layer Base}}, \quad (6)$$

412 and

$$[T_{ICE} + T_{IN}]_{\text{Cloud Base}} \approx [f - P]_{\text{Cloud Base}}. \quad (7)$$

413 Since $f < 0$, the turbulent flux of N_{IN} into the cloud layer plus the turbulent flux of N_{ICE} into
 414 the subcloud layer is always less than precipitation of N_{ICE} at cloud base. In addition, in a

415 slowly evolving state where $T_{IN}|_{\text{Mixed-Layer Base}} > 0$, total IN flux due to sublimation in the
 416 mixed layer, S , can be written as

$$S \approx [P + T_{ICE}]_{\text{Mixed-Layer Base}} - [P + T_{ICE}]_{\text{Cloud Base}} \quad (8a)$$

$$417 \quad \approx [f - T_{IN}]_{\text{Mixed-Layer Base}} - [f - T_{IN}]_{\text{Cloud Base}} \quad (8b)$$

418 and since $f|_{\text{Mixed-Layer Base}}$ is downward and $f|_{\text{Mixed-Layer Top}}$ is negligible (eq. 5),

$$S < T_{IN}|_{\text{Cloud Base}} - T_{IN}|_{\text{Mixed-Layer Base}} \quad (8c)$$

$$< T_{IN}|_{\text{Cloud Base}} \cdot \quad (8d)$$

419 Thus in a well-mixed layer with an upward $T_{IN}|_{\text{Mixed-Layer Base}}$ sublimation is always less than
 420 the flux of N_{IN} into the cloud layer.

421 Based on results from Control, precipitation of N_{ICE} at cloud base is sufficient to balance the
 422 upward turbulent flux of N_{IN} (i.e., $|T_{IN}| \gg |T_{ICE}|$ at cloud base). Therefore, in a well-mixed
 423 layer with precipitation of N_{ICE} at the mixed-layer base that is larger in magnitude than an
 424 upward turbulent N_{IN} flux at the mixed-layer base, and assuming negligible entrainment at
 425 the mixed-layer top

$$|P|_{\text{Cloud Base}} > T_{IN}|_{\text{Cloud Base}} > S. \quad (9)$$

426 However, if all N_{ICE} sublimate in the mixed layer and the upward turbulent flux of N_{IN}
 427 dominates at the mixed-layer base then $f > 0$ and

$$T_{IN}|_{\text{Cloud Base}} > |P|_{\text{Cloud Base}} = S, \quad (10)$$

428 the mixed layer gains $N_{IN} + N_{ICE}$ over time, resulting in a continuously increasing ice
 429 production in the cloud layer. In the presence of shortwave radiation (i.e., in the SW
 430 simulation), $T_{IN}|_{\text{Cloud Base}}$ is also greater than $|P|_{\text{Cloud Base}}$ after a period of weakened
 431 turbulence and weaker precipitation at the mixed-layer base, due to increased activation of
 432 N_{IN} due to decreasing shortwave radiation.

433 If IN entrainment at the mixed-layer top is not negligible then $f(z)$ must be modified to
 434 include fluxes at the mixed-layer top and $|f|_{\text{Cloud Base}}$ will increase. If $|f|_{\text{Cloud Base}}$ increases
 435 such that $f_{\text{Cloud Base}} < P_{\text{Mixed-Layer Base}}$, then sublimation will exceed $T_{IN}|_{\text{Cloud Base}}$.

436 This mixed-layer analysis provides a framework to understand the results presented in
 437 Section 4. Specifically, sublimation being less than the turbulent flux of IN is seen to be a
 438 property of a well-mixed layer where the total flux at mixed-layer base is downward and the
 439 total flux at the mixed-layer top is negligible. In the case where the mixed layer is saturated
 440 with respect to ice, sublimation is equal to zero and the turbulent flux of IN at the mixed-
 441 layer base is less than the turbulent flux of IN at the cloud base, reducing the flux of IN into
 442 the cloud layer. The relationships outlined in this section are appropriate for any AMPS with
 443 weak entrainment at cloud top, weak large-scale advective fluxes, and net downward fluxes
 444 at the mixed-layer base.

445 **6 Analysis of Buffered Feedbacks in SW**

446 Phase diagrams highlight the processes involved in ice production when a diurnal cycle is
447 allowed (following the arrows from green to blue to black to red in Fig. 12a,b). When
448 incoming shortwave radiation is a maximum, recycling (sublimation) is seen to be at a
449 minimum. This is counterintuitive since subcloud relative humidity is low at this time, which
450 would be expected to produce increased sublimation. However, due to weak turbulent mixing
451 between the cloud and subcloud layers the net N_{ICE} flux into the subcloud layer is weak,
452 resulting in weak sublimation and recycling. This situation is reversed as shortwave radiation
453 decreases, since increased cloud-top cooling increases cloud-driven turbulent mixing, which
454 allows recycling to increase in the regions of reduced subcloud relative humidity. As is seen
455 in the conceptual diagram (Fig. 10), this then leads to an increased N_{ICE} flux into the
456 subcloud layer (green arrows, Fig. 12). However, N_{ICE} in the cloud layer doesn't begin to
457 increase until activation in the cloud layer exceeds the flux of N_{ICE} into the subcloud layer
458 (green arrows). This cycle is further amplified as shortwave radiation decreases, namely,
459 decreased shortwave radiation increases cloud-driven turbulence, increasing the flux of IN
460 into the cloud layer, increasing the activation of IN, which increases N_{ICE} in the cloud layer
461 and the N_{ICE} flux from the cloud layer into the subcloud layer (blue arrows).

462 When incoming shortwave radiation is a minimum, more N_{IN} are activated because the cloud
463 layer cools. However, again we see that N_{ICE} tendencies due to thermodynamics are buffered
464 by the slowing of turbulence-driven feedbacks due to a thickening of the cloud layer. Thus, a
465 net increase in N_{ICE} in the cloud layer, commensurate with an increased IWP and
466 precipitation (black arrows), is buffered by a decrease in the downward turbulent mixing of
467 N_{ICE} , which reduces recycling, slowing the feedback loop (see Fig. 10). During the morning
468 hours, as the cloud layer warms and thins and ice activation becomes less efficient,

469 turbulence continues to decline, slowing the recycling feedback process to the point where
470 limited IN fluxes to the cloud layer inhibit ice production and N_{ICE} declines (red arrows).

471 **7 Summary**

472 We have demonstrated that sustained recycling of IN through a drying subcloud layer and
473 additional activation of N_{IN} due to a cooling cloud layer are sufficient to maintain ice
474 production, and regulate liquid production over multiple days in a decoupled AMPS.

475 This study provides an idealized framework to understand feedbacks between dynamics and
476 microphysics that maintain phase-partitioning in AMPS. In addition, we have shown that
477 modulation of the cooling of the cloud layer and the humidity of the subcloud layer by the
478 diurnal cycle buffers the mixed-layer system from a loss of particles and promotes the
479 persistence of a mixed-phase cloud system. The results of this study provide insight into the
480 mechanisms and feedbacks that may maintain cloud ice in AMPS even when entrainment of
481 IN at the mixed-layer boundaries is weak. While the balance of these processes changes
482 depending upon the specific conditions of the cloud layer, for example whether the cloud
483 layer is coupled to the surface layer, the mechanisms detailed in this paper will manifest to
484 some degree and therefore the current study provides a framework for understanding the role
485 of recycling in maintaining phase-partitioning in AMPS.

486 **Author Contributions:**

487 A.S., G.F., and M.D.S. conceived and designed the experiments; A.S. performed the
488 simulations; A.S., G.F., and M.D.S. analyzed the model results and co-wrote the paper.

489 **Acknowledgements:**

490 The authors acknowledge discussions with Alex Avramov, Chris Cox, Gijs de Boer, Barbara
491 Ervens, and Ann Fridlind, and Takanobu Yamaguchi for developing the software to run
492 WRF as a large eddy simulation. This research was supported by the Office of Science
493 (BER), U.S. Department of Energy (DE-SC0011918) and the National Science Foundation
494 (ARC-1023366).

495 **References**

- 496 Abdul-Razzak, H. and Ghan, S. J.: A parameterization of aerosol activation 2. Multiple
497 aerosol types, *J. Geophys. Res.*, 105, 6837–6844, 2000.
- 498 Avramov, A., Ackerman, A. S., Fridlind, A. M., van Diedenhoven, B., Botta, G., Aydin, K.,
499 Verlinde, J., Korolev, A. V., Strapp, J. W., McFarquhar, G. M., Jackson, R., Brooks, S.
500 D., Glen, A., and Wolde, M.: Toward ice formation closure in Arctic mixed-phase
501 boundary layer clouds during ISDAC, *J. Geophys. Res.*, 116, D00T08,
502 doi:10.1029/2011JD015910, 2011.
- 503 Barton, N. P., Klein, S. A., Boyle, J. S., and Zhang, Y. Y.: Arctic synoptic regimes:
504 Comparing domain wide Arctic cloud observations with CAM4 and CAM5 during
505 similar dynamics, *J. Geophys. Res.*, 117, D15205, doi:10.1029/2012JD017589, 2012.
- 506 Bennartz, R., Shupe, M., Turner, D., Walden, V., Steffen, K., Cox, C., Kulie, M. S., Miller,
507 N., and Pettersen, C.: July 2012 Greenland melt extent enhanced by low-level liquid
508 clouds, *Nature*, 496, 83-86, doi:10.1038/nature12002, 2012.
- 509 Birch, C. E., Brooks, I. M., Tjernström, M., Shupe, M. D., Mauritsen, T., Sedlar, J., Lock, A.
510 P., Earnshaw, P., Persson, P. O. G., Milton, S. F., and Leck, C.: Modeling atmospheric
511 structure, cloud and their response to CCN in the central Arctic: ASCOS case studies,
512 *Atmos. Chem. Phys.*, 12, 3419-3435, doi:10.5194/acp-12-3419-2012, 2012.
- 513 Bretherton, C. S. and Wyant, M. C.: Moisture transport, lower-tropospheric stability, and
514 decoupling of cloud-topped boundary layers, *J. Atmos. Sci.*, 54, 148-167, 1997.
- 515 Broadley, S., Murray, B., Herbert, R., Atkinson, J., Dobbie, S., Malkin, T., Condliffe, E., and
516 Neve, L.: Immersion mode heterogeneous ice nucleation by an illite rich powder
517 representative of atmospheric mineral dust, *Atmos. Chem. Phys.*, 12:287{307,

518 doi:10.5194/acp-12-287-2012, 2012.

519 Chen, J.-P. and Lamb, D.: The theoretical basis for the parameterization of ice crystal habits:
520 Growth by vapor deposition, *J. Atmos. Sci.*, 51, 1206–1222, doi:10.1175/1520-
521 0469(1994)051<1206:TTBFTP>2.0.CO;2, 1994.

522 Collins, W. D., Rasch, P. J., Boville, B. A., Hack, J. J., McCaa, J. R., Williamson, D. L., and
523 Briegleb, B. P.: Description of the NCAR Community Atmosphere Model (CAM 3.0),
524 NCAR Technical Note, NCAR/TN-464+STR, 226 pp., 2004.

525 Curry, J. and Ebert, E. E.: Annual cycle of radiation fluxes over the Arctic Ocean: Sensitivity
526 to cloud optical properties, *J. Climate*, 5, 1267–1280, 1992.

527 Cziczo, D., Froyd, K., Gallavardin, S., Moehler, O., Benz, S., Saathoff, H., and Murphy, D.:
528 Deactivation of ice nuclei due to atmospherically relevant surface coatings, *Environ.*
529 *Res. Lett.*, 4:044013, doi:10.1088/1748-9326/4/4/044013, 2009.

530 de Boer, G., Chapman, W., Kay, J. E., Medeiros, B., Shupe, M. D., Vavrus, S., and Walsh, J.:
531 A characterization of the present-day Arctic atmosphere in CCSM4, *J. Climate*, 25,
532 2676–2695, 2012.

533 DeMott, P. J.: An exploratory study of ice nucleation by soot aerosols, *J. Appl. Meteorol.*,
534 29(10), 1072–1079, 1990.

535 DeMott, P. J., Prenni, A. J., Liu, X., Petters, M. D., Twohy, C. H., Richardson, M. S.,
536 Eidhammer, T., Kreidenweis, S. M., and Rogers, D. C.: Predicting global atmospheric
537 ice nuclei distributions and their impacts on climate, *P. Natl. Acad. Sci. USA*, 107,
538 11217–11222, doi:10.1073/pnas.0910818107, 2010.

539 Dyer, A. J. and Hicks, B. B.: Flux-gradient relationships in the constant flux layer, *Q. J. Roy.*
540 *Meteor. Soc.*, 96, 715–721, 1970.

541 Ervens, B., Feingold, G., Sulia, K., and Harrington, J.: The impact of microphysical
542 parameters, ice nucleation mode, and habit growth on the ice/liquid partitioning in
543 mixed-phase Arctic clouds, *J. Geophys. Res.*, 116, D17205,
544 doi:10.1029/2011JD015729, 2011.

545 Fan, J., Ovchinnikov, M., Comstock, J. M., McFarlane, S. A., and Khain, A.: Ice formation
546 in Arctic mixed-phase clouds: Insights from a 3-D cloud-resolving model with size-
547 resolved aerosol and cloud microphysics, *J. Geophys. Res.*, 114, D04205,
548 doi:10.1029/2008JD010782, 2009.

549 Feingold, G., Kreidenweis, S. M., Stevens, B., and Cotton, W. R.: Numerical simulation of
550 stratocumulus processing of cloud condensation nuclei through collision-coalescence, *J.*
551 *Geophys. Res.*, 101, 21,391-21,402, 1996.

552 Fridlind, A. M., van Diedenhoven, B., Ackerman, A. S., Avramov, A., Mrowiec, A.,
553 Morrison, H., Zuidema, P., and Shupe, M. D.: A FIRE-ACE/SHEBA case study of
554 mixed-phase Arctic boundary-layer clouds: Entrainment rate limitations on rapid
555 primary ice nucleation processes, *J. Atmos. Sci.*, 69, 365-389, doi:10.1175/JAS-D-11-
556 052.1, 2012.

557 Hobbs, P. V. and Rangno A. L.: Microstructure of low and middle- level clouds over the
558 Beaufort Sea, *Q. J. Roy. Meteor. Soc.*, 124, 2035-2071, 1998.

559 Hoose, C. and Möhler, O.: Heterogeneous ice nucleation on atmospheric aerosols: a review
560 of results from laboratory experiments, *Atmos. Chem. Phys.*, 12, 9817-9854,
561 doi:10.5194/acp-12-9817-2012, 2012.

562 Iacono, M. J., Delamere, J. S., Mlawer, E. J., Shephard, M. W., Clough, S. A., and Collins,
563 W. D.: Radiative forcing by long-lived greenhouse gases: Calculations with the AER

564 Radiative transfer models, *J. Geophys. Res.*, 113, D13103, doi:10.1029/2008JD009944,
565 2008.

566 Intrieri, J. M., Fairall, C. W., Shupe, M. D., Persson, P. O. G., Andreas, E., Guest, P. S., and
567 Moritz, R. E.: An annual cycle of Arctic surface cloud forcing at SHEBA, *J. Geophys.*
568 *Res.*, 107, 8039, doi:10.1029/2000JC000439, 2002.

569 Kanji, Z., DeMott, P., Möhler, O., and Abbatt, J.: Results from the University of Toronto
570 continuous flow diffusion chamber at ICIS 2007: instrument intercomparison and ice
571 onsets for different aerosol types, *Atmos. Chem. Phys.*, 11:31-41, doi:10.5194/acp-11-
572 31-2011, 2011.

573 Karlsson, J. and Svensson, G.: The simulation of Arctic clouds and their influence on the
574 winter surface temperature in present-day climate in the CMIP3 multi-model dataset,
575 *Clim. Dynam.*, 36, 623–635, 2011.

576 Klein, S. A., McCoy, R., Morrison, H., Ackerman, A., Avramov, A., de Boer, G., Chen, M.,
577 Cole, J., DelGenio, A. D., Falk, M., Foster, M., Fridlind, A., Golaz, J.-C., Hashino, T.,
578 Harrington, J., Hoose, C., Khairoutdinov, M., Larson, V., Liu, X., Luo, Y., McFarquhar,
579 G., Menon, S., Neggers, R., Park, S., von Salzen, K., Schmidt, J. M., Sednev, I.,
580 Shipway, B., Shupe, M., Spangenberg, D., Sud, Y., Turner, D., Veron, D., Walker, G.,
581 Wang, Z., Wolf, A., Xie, S., Xu, K.-M., Yang, G., and Zhang, G.: Intercomparison of
582 model simulations of mixed-phase clouds observed during the ARM Mixed-Phase Arctic
583 Cloud Experiment. I: Single-layer cloud, *Q. J. Roy. Meteor. Soc.*, 135, 979–1002, 2009.

584 Korolev, A.: Limitations of the Wegener–Bergeron–Findeisen mechanism in the evolution of
585 mixed-phase clouds, *J. Atmos. Sci.*, 64, 3372–3375, doi:10.1175/JAS4035.1, 2007.

586 Korolev, A. and Sussman, B.: A technique for habit classification of cloud particles, *J. Atmos.*
587 *Oceanic Technol.*, 17, 1048–1057, 2000.

588 Kulkarni, G., Fan, J., Comstock, J., Liu, X., and Ovchinnikov, M.: Laboratory measurements
589 and model sensitivity studies of dust deposition ice nucleation, *Atmos. Chem. Phys.*,
590 12:7295-7308, doi:10.5194/acp-12-7295-2012, 2012.

591 Levin, Z. and Yankofsky, S.: Contact versus immersion freezing of freely suspended droplets
592 by bacterial ice nuclei, *J. Appl. Meteorol. Clim.*, 22, 1964-1966, 1983.

593 Lilly, D. K.: Models of cloud-topped mixed layers under a strong inversion, *Q. J. Roy.*
594 *Meteor. Soc.*, 94, 292–309, 1968.

595 Lüönd, F., Stetzer, O., Welti, A., and Lohmann, U.: Experimental study on ice nucleation
596 ability of size selected kaolinite particles in the immersion mode, *J. Geophys. Res.*,
597 115:D14201, doi:10.1029/2009JD012959, 2010.

598 McFarquhar, G. M., Zhang, G., Poellot, M. R., Kok, G. L., McCoy, R., Tooman, T., Fridlind,
599 A., and Heymsfield, A. J.: Ice properties of single-layer stratocumulus during the Mixed-
600 Phase Arctic Cloud Experiment: 1. Observations, *J. Geophys. Res.*, 112, D24201,
601 doi:10.1029/2007JD008633, 2007.

602 McFarquhar, G. M., Ghan, S., Verlinde, J., Korolev, A., Strapp, J. W., Schmid, B.,
603 Tomlinson, J. M., Wolde, M., Brooks, S. D., Cziczo, D., Dubey, M. K., Fan, J., Flynn,
604 C., Gultepe, I., Hubbe, J., Gilles, M. K., Laskin, A., Lawson, P., Leitch, W. R., Liu, P.,
605 Liu, X., Lubin, D., Mazzoleni, C., Macdonald, A.-M., Moffet, R. C., Morrison, H.,
606 Ovchinnikov, M., Shupe, M. D., Turner, D. D., Xie, S., Zelenyuk, A., Bae, K., Freer, M.,
607 and Glen, A.: Indirect and Semi-Direct Aerosol Campaign (ISDAC): The Impact of

608 Arctic Aerosols on Clouds, *B. Am. Meteorol. Soc.*, 92, 183–201,
609 doi:10.1175/2010BAMS2935.1, 2011.

610 Möhler, O., Büttner, S., Linke, C., Schnaiter, M., Saathoff, H., Stetzer, O., Wagner, R.,
611 Krämer, M., Mangold, A., Ebert, V., and Schurath, U.: Effect of sulfuric acid coating on
612 heterogeneous ice nucleation by soot aerosol particles, *J. Geophys. Res.*, 110:D11210,
613 doi: 10.1029/2004JD005169, 2005.

614 Möhler, O., Field, P., Connolly, P., Benz, S., Saathoff, H., Schnaiter, M., Wagner, R., Cotton,
615 R., Krämer, M., Mangold, A., and Heymsfield, A.: Efficiency of the deposition mode ice
616 nucleation on mineral dust particles, *Atmos. Chem. Phys.*, 6:3007-3021,
617 doi:10.5194/acp-6-3007-2006, 2006.

618 Morrison, H. and Pinto, J. O.: Mesoscale modeling of springtime Arctic mixed-phase
619 stratiform clouds using a new two-moment bulk microphysics scheme, *J. Atmos. Sci.*, 62,
620 3683-3704, 2005.

621 Morrison, H., Thompson, G., and Tatarskii, V.: Impact of cloud microphysics on the
622 development of trailing stratiform precipitation in a simulated squall line: Comparison of
623 one- and two-moment schemes, *Mon. Wea. Rev.*, 137, 991-1007,
624 doi:10.1175/2008MWR2556.1, 2009.

625 Paulson, C. A.: The mathematical representation of wind speed and temperature profiles in
626 the unstable atmospheric surface layer, *J. Appl. Meteor.*, 9, 857–861, 1970.

627 Persson, P. O. G.: Onset and end of the summer melt season over sea ice: Thermal structure
628 and surface energy perspective from SHEBA, *Clim. Dynam.*, 39, 1349-1371,
629 doi:10.1007/s00382-011-1196-9, 2012.

630 Pinti, V., Marcolli, C., Zobrist, B., Hoyle, C., and Peter, T.: Ice nucleation efficiency of clay
631 minerals in the immersion mode, *Atmos. Chem. Phys.*, 12:5859-5878, doi:10.5194/acp-
632 12-5859-2012, 2012.

633 Pruppacher, H. and Klett, J.: *Microphysics of clouds and precipitation*. Kluwer Academic
634 Publishers, 2nd edition, 1997.

635 Roberts, P. and Hallett, J.: A laboratory study of the ice nucleating properties of some
636 mineral particulates, *Q. J. R. Meteorol. Soc.*, 94, 25 – 34, 1967.

637 Sandvik, A., Biryulina, M., Kvamsto, N., Stamnes, J., and Stamnes, K.: Observed and
638 simulated microphysical composition of Arctic clouds: Data properties and model
639 validation, *J. Geophys. Res.* 112, D05205, 2007.

640 Sedlar, J., Shupe, M. D., and Tjernström, M.: On the relationship between thermodynamic
641 structure, cloud top, and climate significance in the Arctic, *J. Climate*, 25, 2374–2393,
642 2012.

643 Sedlar, J., Tjernström, M., Mauritsen, T., Shupe, M. D., Brooks, I. M., Persson, P. O. G.,
644 Birch, C. E., and C. Leck, C.: A transitioning Arctic surface energy budget: The impacts
645 of solar zenith angle, surface albedo and cloud radiative forcing, *Clim. Dynam.*, 37,
646 1643–1660, doi:10.1007/s00382-010-0937-5, 2011.

647 Serreze, M. C., Barrett, A. P., and Stroeve, J.: Recent changes in tropospheric water vapor
648 over the Arctic as assessed from radiosondes and atmospheric reanalyses. *J. Geophys.*
649 *Res.*, 117, D10104, doi:10.1029/2011JD017421, 2012.

650 Sheridan, L. M., Harrington, J. Y., Lamb, D., and Sulia, K.: Influence of ice crystal aspect
651 ratio on the evolution of ice size spectra during vapor depositional growth, *J. Atmos. Sci.*,
652 66, 3732–3743, doi:10.1175/2009JAS3113.1, 2009.

653 Shupe, M. D.: A ground-based multiple remote-sensor cloud phase classifier, *Geophys. Res.*
654 *Lett.*, 34, L2209, doi:10.1029/2007GL031008, 2007.

655 Shupe, M. D and J. M. Intrieri: Cloud radiative forcing of the Arctic surface: The influence
656 of cloud properties, surface albedo, and solar zenith angle, *J. Climate*, 17, 616-628, 2004.

657 Shupe, M. D, Matrosov, S. Y., and Uttal, T.: Arctic mixed phase cloud properties derived
658 from surface-based sensors at SHEBA, *J. Atmos. Sci.*, 63, 697-811, 2006.

659 Shupe, M. D, Persson, P. O. G., Brooks, I. M., Tjernström, M., Sedlar, J., Mauritsen, T.,
660 Sjogren, S., and Leck, C.: Cloud and boundary layer interactions over the Arctic sea-ice
661 in late summer, *Atmos. Chem. Phys.*, 13, 9379-9400, 2013.

662 Skamarock, W. C., Klemp, J. B., Dudhia, J., Gill, D. O., Barker, D. M., Duda, M. G., Huang,
663 X.-Y., Wang, W., and Powers, J. G.: A description of the Advanced Research WRF
664 version 3, NCAR Tech. Note NCAR/TN-475+STR, 113 pp., 2008.

665 Solomon, A., Morrison, H., Persson, P. O. G., Shupe, M. D., and Bao, J.-W.: Investigation of
666 microphysical parameterizations of snow and ice in Arctic clouds during M-PACE
667 through model-observation comparisons, *Mon. Wea. Rev.*, 137, 3110-3128,
668 doi:10.1175/2009MWR2688.1, 2009.

669 Solomon, A., Shupe, M. D., Persson, P. O. G., and Morrison, H.: Moisture and dynamical
670 interactions maintaining decoupled Arctic mixed-phase stratocumulus in the presence of
671 a humidity inversion, *Atmos. Chem. Phys.*, 11, 10127-10148, doi:10.5194/acp-11-10127-
672 2011, 2011.

673 Solomon, A., Shupe, M. D., Persson, P. O. G., Morrison, H., Yamaguchi, T., Caldwell, P. M.,
674 and de Boer, G.: The sensitivity of springtime Arctic mixed-phase stratocumulus clouds

675 to surface layer and cloud-top inversion layer moisture sources, *J. Atmos. Sci.*, 71, 574-
676 595, doi:10.1175/JAS-D-13-0179.1, 2014.

677 Tjernström, M., Sedlar, J., and Shupe, M. D.: How well do regional climate models
678 reproduce radiation and clouds in the Arctic? An evaluation of ARCMIP simulations, *J.*
679 *Appl. Met. Clim.*, 47, 2405–2422, 2008.

680 Tjernström, M., C. Leck, C., Persson, P. O. G., Jensen, M. L., Oncley, S. P., and Targino, A.:
681 The summertime Arctic atmosphere: Meteorological measurements during the Arctic
682 Ocean Experiment 2001, *B. Am. Meteorol. Soc.*, 85, 1305–1321, 2004.

683 Turner, D. D., Clough, S. A., Liljegren, J. C., Clothiaux, E. E., Cady-Pereira, K., and Gaustad,
684 K. L.: Retrieving precipitable water vapor and liquid water path from Atmospheric
685 Radiation Measurement (ARM) program’s microwave radiometers, *IEEE T. Geosci.*
686 *Remote*, 45, 3680–3690, 2007.

687 Verlinde, J., Harrington, J. Y., McFarquhar, G. M., et al.: The Mixed-Phase Arctic Cloud
688 Experiment (M-PACE), *B. Am. Meteorol. Soc.*, 88, 205–221, doi:10.1175/BAMS-88-2-
689 205, 2007.

690 Walsh, J. E. and Chapman, W. L.: Arctic cloud-radiation temperature associations in
691 observational data and atmospheric reanalyses, *J. Climate*, 11, 3030–3045, 1998.

692 Webb, E. K.: Profile relationships: The log-linear range, and extension to strong stability.
693 *Quart. J. Roy. Meteor. Soc.*, 96, 67–90, 1970.

694 Wise, M., Baustian, K., Koop, T., Freedman, M., Jensen, E., and Tolbert, M.: Depositional
695 ice nucleation onto crystalline hydrated nacl particles: a new mechanism for ice
696 formation in the troposphere, *Atmos. Chem. Phys.*, 12:1121-1134, doi:10.5194/acp-12-
697 1121-2012, 2012.

698 Yamaguchi, T. and Feingold, G.: Technical note: Large-eddy simulation of cloudy boundary
699 layer with the Advanced Research WRF model, *J. Adv. Model. Earth Syst.*, 4, M09003,
700 doi:10.1029/2012MS000164, 2012.

701 **Figure Captions**

702 **Figure 1:** Sounding measured at 17:34 UTC 8 April 2008 at Barrow, Alaska (71.338N,
703 156.68W). Left) Water vapor mixing ratio (q_v), temperature (T), and potential temperature
704 (Theta), in units of g kg^{-1} , degrees Kelvin, and degrees Kelvin respectively. Right) Zonal
705 wind (U) and meridional wind (V), in units of m s^{-1} . Gray shading marks the extent of the
706 cloud layer. The dashed lines show the initial profiles used in the WRFLES experiments. The
707 dashed line overlaying water vapor mixing ratio is the initial profile for the total water
708 mixing ratio.

709 **Figure 2:** IN number concentration active at water saturation vs. temperature based on the
710 empirical relationship derived in DeMott et al. (2010) (blue line) used to initialize IN number
711 concentration in each bin. Black vertical lines indicate threshold temperatures for nucleation
712 in the 16 IN bins. Note additional IN become available for nucleation at colder temperatures,
713 such that, for example, at -20.2°C (the coldest temperature in the Control simulation) the total
714 number of IN available for activation is $\sim 1.5 \text{ L}^{-1}$.

715 **Figure 3:** Sensitivity of ice water path to the parameter F in equation (2). Note the similar ice
716 water paths for $F=4$ and $F=6$ (total N_{IN} initial values 5.8 and 8.7 L^{-1} , respectively).

717 **Figure 4:** A,B,D) Sensitivity of LWP and IWP to snow density and fall speeds. LWP shown
718 with solid lines and IWP shown with dashed lines, in units of g m^{-2} . C) Fall speeds used in
719 sensitivity studies, in units of m s^{-1} . A) Sensitivity to reducing snow density from 100 kg m^{-3}
720 to 50 kg m^{-3} (red lines) using Control (CNT) fall speeds (red line in C). B) Sensitivity to
721 reducing snow fall speeds (green line in C) using Control snow density (red lines). D)
722 Sensitivity to increasing snow fall speeds (blue line in C) using Control snow density (red

723 lines).

724 **Figure 5:** Simulated ice particle number size distributions using in-cloud mass and number
725 concentrations. Ice water mixing ratio = $3\text{e-}4$ g/kg, ice number concentration = $0.4/\text{L}$, snow
726 water mixing ratio = $2.4\text{e-}2$ g/kg, snow number concentration = $0.45/\text{L}$.

727 **Figure 6:** (A) N_{IN} and (B) N_{ICE} averaged over 0.5 hours at hour 20, in units of $\text{L}^{-1} \text{hr}^{-1}$. Grey
728 shading indicates the extent of the cloud layer. Green dash lines indicate the top and bottom
729 of the mixed layer.

730 **Figure 7:** Time-height cross sections of horizontally-averaged (A) IN advection plus
731 subsidence, in units of $\text{L}^{-1}\text{hour}^{-1}$, (B) ice plus snow number concentration, in units of L^{-1} , (C)
732 water vapor mixing ratio, in units of g kg^{-1} , and (D) relative humidity with respect to ice, in
733 units of percent, from CNT simulation. Temperature, in units of $^{\circ}\text{C}$, shown with black
734 contour lines in (B,C,D).

735 **Figure 8:** Control and NoRecycle time series for hours 6-40 (smoothed with 90 minute
736 running average). NoRecycle shown with red and black dashed lines. A) LWP (black) and
737 IWP (red), in units of g m^{-2} . B) Minimum horizontally-averaged temperature in the column,
738 in units of $^{\circ}\text{C}$. C) Mixed-layer depth (blue), top height (red), and base height (black), in units
739 of km. D) N_{ICE} integrated over cloud layer (referred to as CL, red) and N_{IN} integrated over
740 subcloud layer (referred to as SubCL, black), in units of m L^{-1} (i.e., meters/liter).

741 **Figure 9:** Horizontally-averaged fluxes from Control and NoRecycle integrations for hours
742 6-40 (smoothed with 90 minute running average). NoRecycle shown with red and black
743 dashed lines. A) N_{ICE} flux at cloud base due to turbulence+subsidence+precipitation (red),

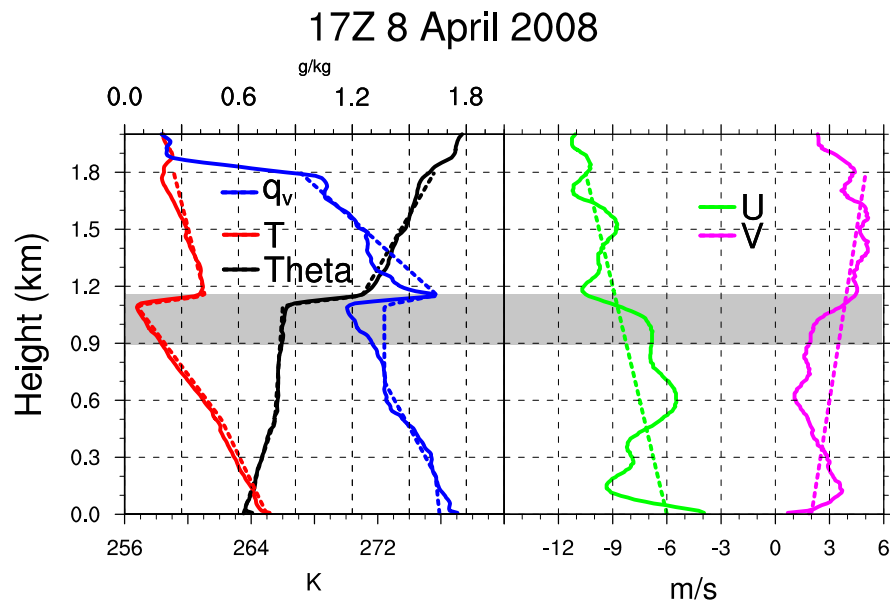
744 mixed-layer base due to turbulence+subsidence+precipitation (black), and due to activation
745 (multiplied by -1, blue), in units of $\text{m L}^{-1} \text{hr}^{-1}$. B) N_{IN} flux at cloud base (indicated by CB in
746 legend) due to turbulence (red), N_{IN} flux due to sublimation (black), and precipitation of N_{ICE}
747 at cloud base (multiplied by -1, blue), in units of $\text{m L}^{-1} \text{hr}^{-1}$. C) N_{IN} entrainment at mixed-
748 layer top (red) and base (black), in units of $\text{m L}^{-1} \text{hr}^{-1}$.

749

750 **Figure 10:** Schematic of feedback loops that maintain ice production and the phase-
751 partitioning between cloud liquid and ice in an AMPS. Red colors denote N_{IN} . Blue colors
752 denote N_{ICE} . The size of the arrow indicates the relative magnitude of the flux. Vertical
753 profiles of N_{ICE} , N_{IN} , relative humidity, and temperature shown with thin blue, red, green, and
754 yellow lines, respectively.

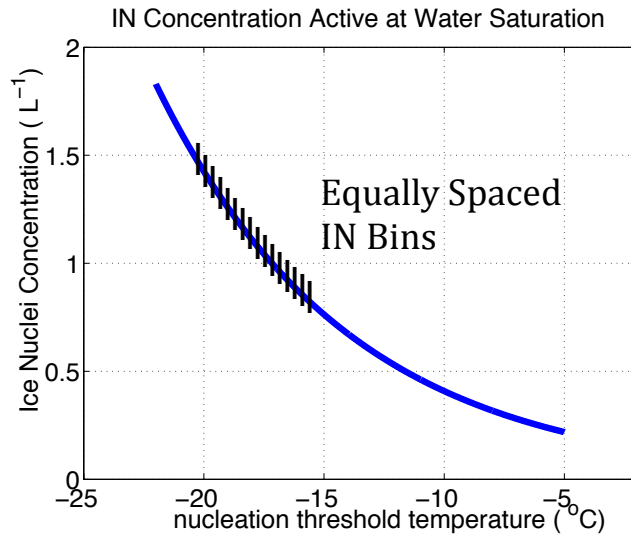
755 **Figure 11:** A) LWP (black) and IWP (red), in units of g m^{-2} . (B) Downward surface
756 shortwave radiation and turbulent kinetic energy (TKE) at cloud base, in units of Wm^{-2} and
757 m^2s^{-2} , respectively. C) N_{ICE} in cloud layer (referred to as CL, red) and N_{IN} in subcloud layer
758 (referred to as SubCL, black), in units of m L^{-1} . (D) Total, turbulent, precipitation N_{ICE} flux at
759 cloud base (referred to as CL base, red, green, blue, respectively) and total N_{ICE} flux at
760 mixed-layer base (referred to as ML base, black), in units of $\text{m L}^{-1} \text{hr}^{-1}$, for the SW
761 integration for hours 16-76. Grey shading indicates hours with zero downwelling surface
762 shortwave radiation. E) N_{IN} entrainment at mixed-layer top (red) and base (black), in units of
763 $\text{m L}^{-1} \text{hr}^{-1}$. (F) N_{IN} flux at cloud base due to turbulence (red), N_{IN} flux due to sublimation
764 (black), and activation of N_{ICE} (blue), in units of $\text{m L}^{-1} \text{hr}^{-1}$.

765 **Figure 12:** A) Phase diagram of TKE at cloud base vs. N_{ICE} in the cloud layer starting at
766 peak shortwave hour 40, in units of m L^{-1} and $\text{m L}^{-1} \text{hr}^{-1}$, respectively. Colors show
767 sublimation in units of $\text{m L}^{-1} \text{hr}^{-1}$. H) 24-hour phase diagrams of sublimation vs. minimum
768 relative humidity in the subcloud layer starting at peak shortwave hour 40, in units of m L^{-1}
769 hr^{-1} and %, respectively. Colors show total N_{ICE} flux at cloud base, $\text{m L}^{-1} \text{hr}^{-1}$. Hours 42-47,
770 47-50, 50-56, and 57-62 indicated with green, blue, black, red arrows, respectively.
771 Minimum shortwave indicated with the moon symbol. Maximum shortwave indicated with
772 the sun symbol.



773 **Figure 1:** Sounding measured at 17:34 UTC 8 April 2008 at Barrow, Alaska (71.338N,
 774 156.68W). Left) Water vapor mixing ratio (q_v), temperature (T), and potential temperature
 775 (Θ), in units of g kg^{-1} , degrees Kelvin, and degrees Kelvin respectively. Right)
 776 zonal wind (U) and meridional wind (V), in units of m s^{-1} . Gray shading marks the extent of the
 777 cloud layer. The dashed lines show the initial profiles used in the WRFLES experiments. The
 778 dashed line overlaying water vapor mixing ratio is the initial profile for the total water
 779 mixing ratio.

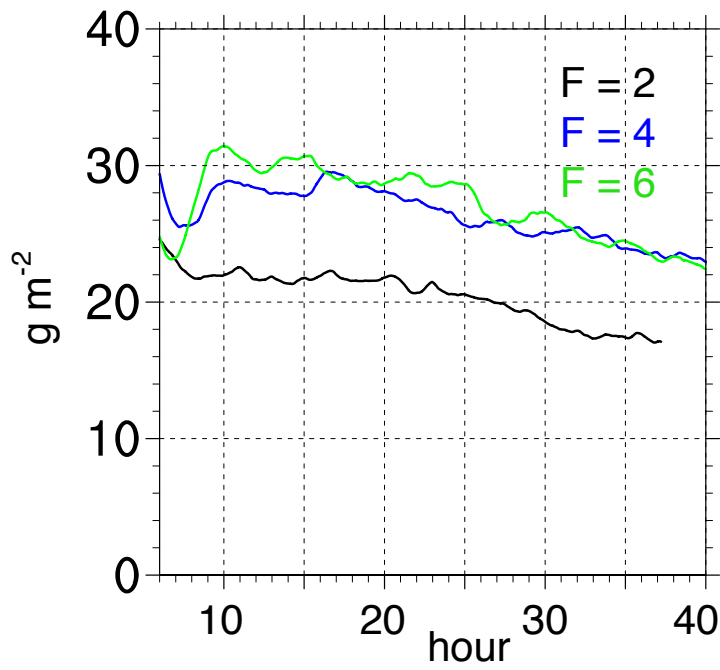
780



781
782

783 **Figure 2:** IN number concentration active at water saturation vs. temperature based on the
784 empirical relationship derived in DeMott et al. (2010) (blue line) used to initialize IN number
785 concentration in each bin. Black vertical lines indicate threshold temperatures for nucleation
786 in the 16 IN bins. Note additional IN become available for nucleation at colder temperatures,
787 such that, for example, at -20.2°C (the coldest temperature in the Control simulation) the total
788 number of IN available for activation is ~1.5 L⁻¹.

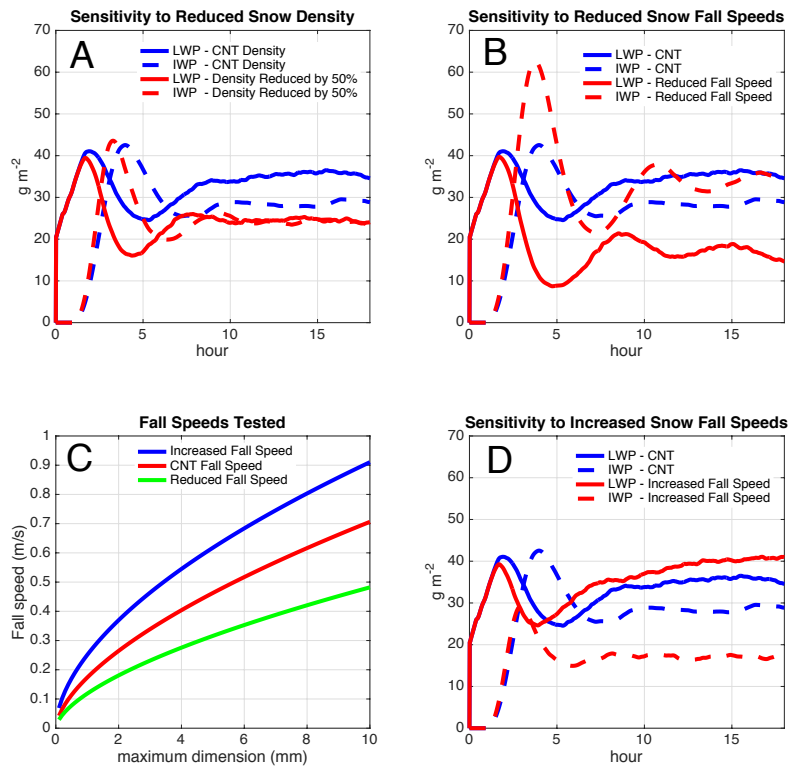
Ice Water Paths



789

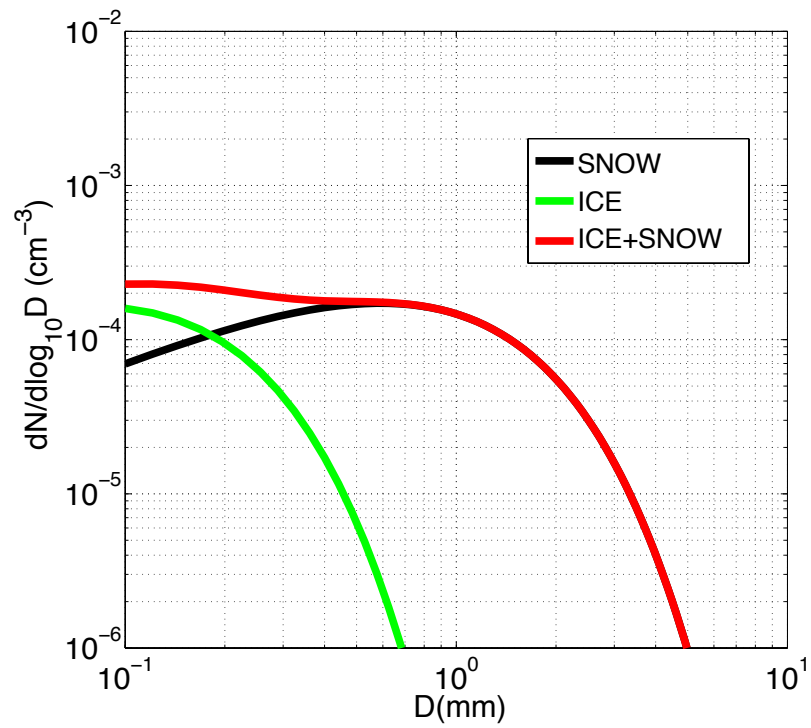
790 **Figure 3:** Sensitivity of ice water path to the parameter F in equation (2). Note the similar ice

791 water paths for $F=4$ and $F=6$ (total N_{IV} initial values of 5.8 and 8.7 L^{-1} , respectively).



792

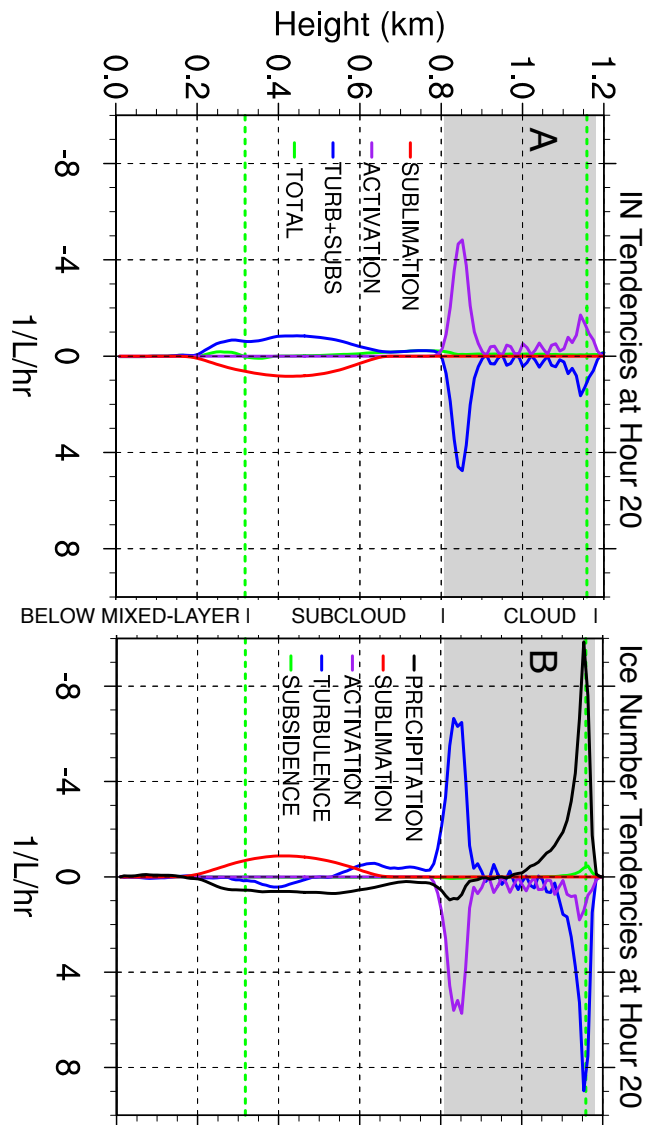
793 **Figure 4:** A,B,D) Sensitivity of LWP and IWP to snow density and fall speeds. LWP shown
 794 with solid lines and IWP shown with dashed lines, in units of $g\ m^{-2}$. C) Fall speeds used in
 795 sensitivity studies, in units of $m\ s^{-1}$. A) Sensitivity to reducing snow density from $100\ kg\ m^{-3}$
 796 to $50\ kg\ m^{-3}$ (red lines) using Control (CNT) fall speeds (red line in C). B) Sensitivity to
 797 reducing snow fall speeds (green line in C) using Control snow density (red lines). D)
 798 Sensitivity to increasing snow fall speeds (blue line in C) using Control snow density (red
 799 lines).



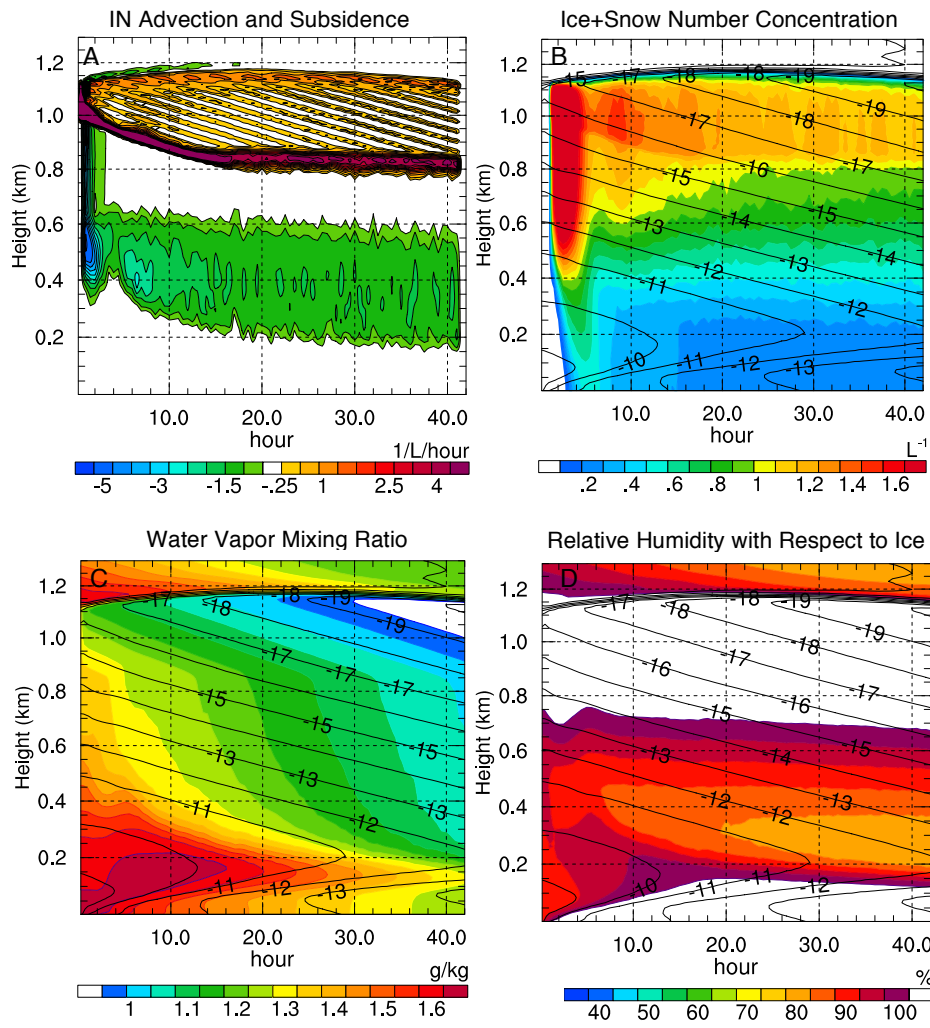
800

801 **Figure 5:** Simulated ice particle number size distributions using in-cloud mass and number
 802 concentrations. Ice water mixing ratio = $3e-4$ g/kg, ice number concentration = 0.4/L, snow
 803 water mixing ratio = $2.4e-2$ g/kg, snow number concentration = 0.45/L.

804



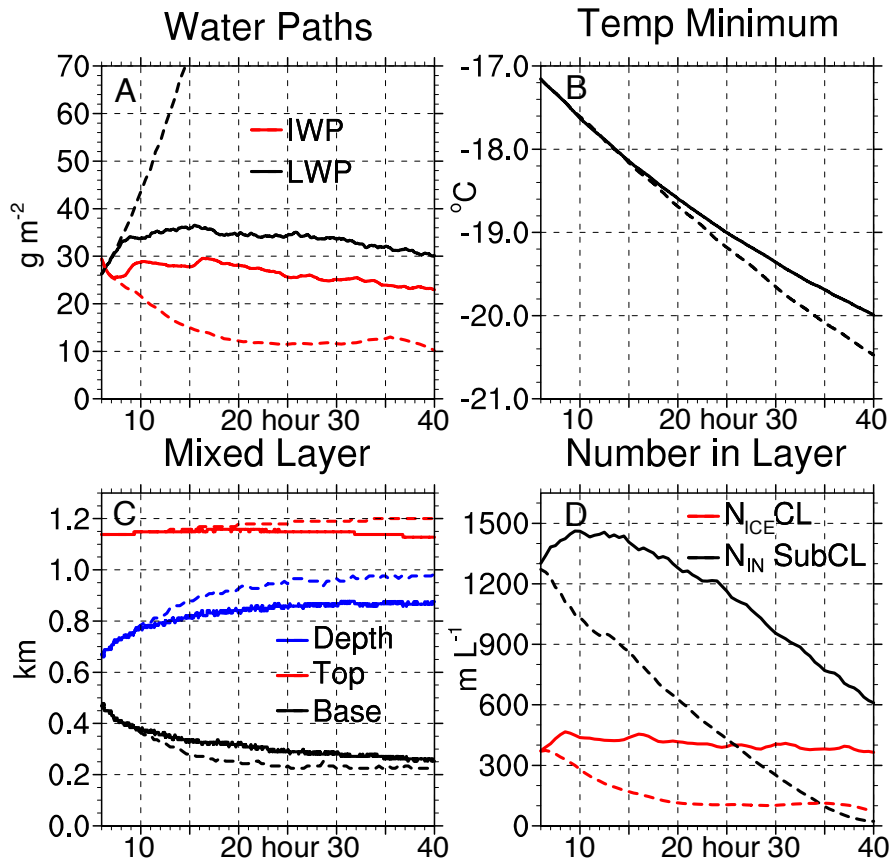
806 **Figure 6:** (A) N_{IN} and (B) N_{ICE} averaged over 0.5 hours at hour 20, in units of $L^{-1} hr^{-1}$. Grey
 807 shading indicates the extent of the cloud layer. Green dash lines indicate the top and bottom
 808 of the mixed layer.



809

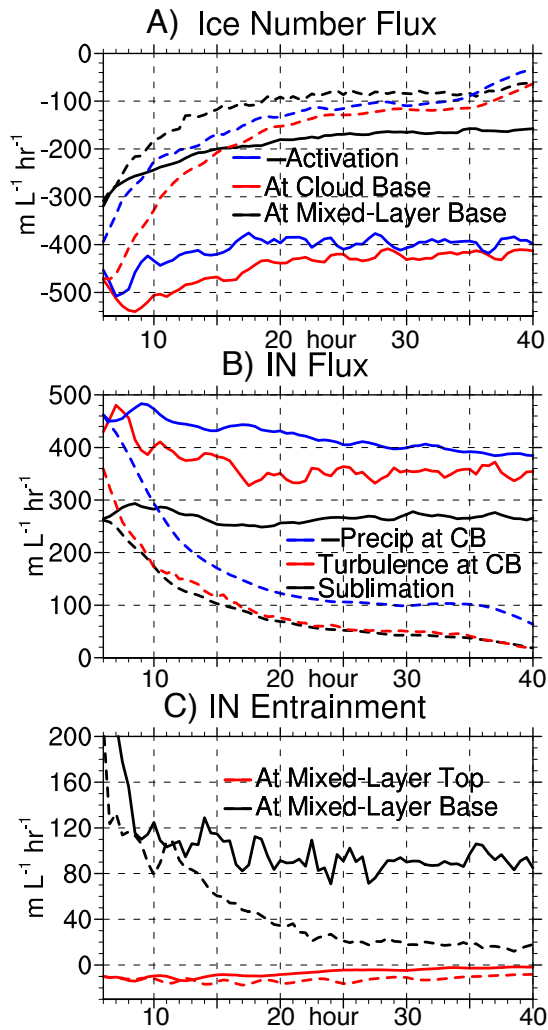
810

811 **Figure 7:** Time-height cross sections of horizontally-averaged (A) IN advection plus
 812 subsidence, in units of $L^{-1}hour^{-1}$, (B) ice plus snow number concentration, in units of L^{-1} , (C)
 813 water vapor mixing ratio, in units of $g kg^{-1}$, and (D) relative humidity with respect to ice, in
 814 units of percent, from CNT simulation. Temperature, in units of $^{\circ}C$, shown with black
 815 contour lines in (B,C,D).



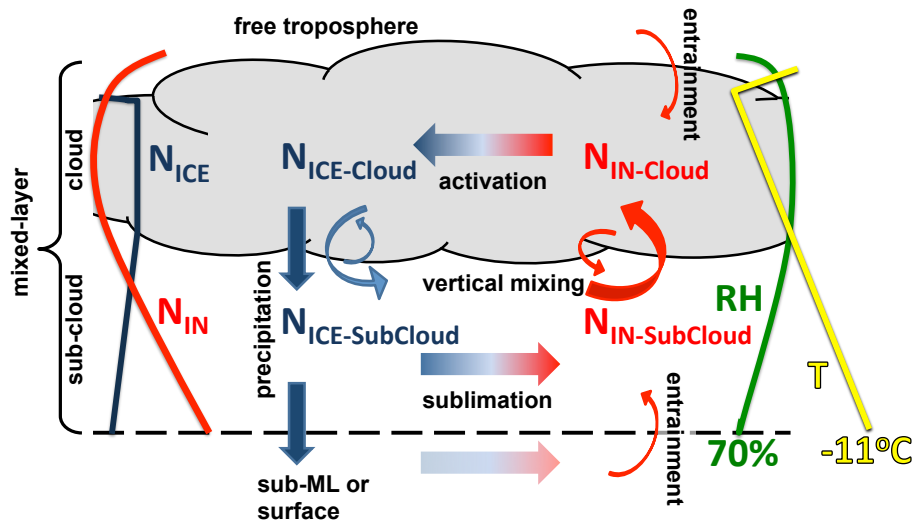
817

818 **Figure 8:** Control and NoRecycle time series for hours 6-40 (smoothed with 90 minute
 819 running average). NoRecycle shown with red and black dashed lines. A) LWP (black) and
 820 IWP (red), in units of g m^{-2} . B) Minimum horizontally-averaged temperature in the column,
 821 in units of $^{\circ}\text{C}$. C) Mixed-layer depth (blue), top height (red), and base height (black), in units
 822 of km. D) N_{ICE} integrated over cloud layer (referred to as CL, red) and N_{IN} integrated over
 823 subcloud layer (referred to as SubCL, black), in units of m L^{-1} (i.e., meters/liter).



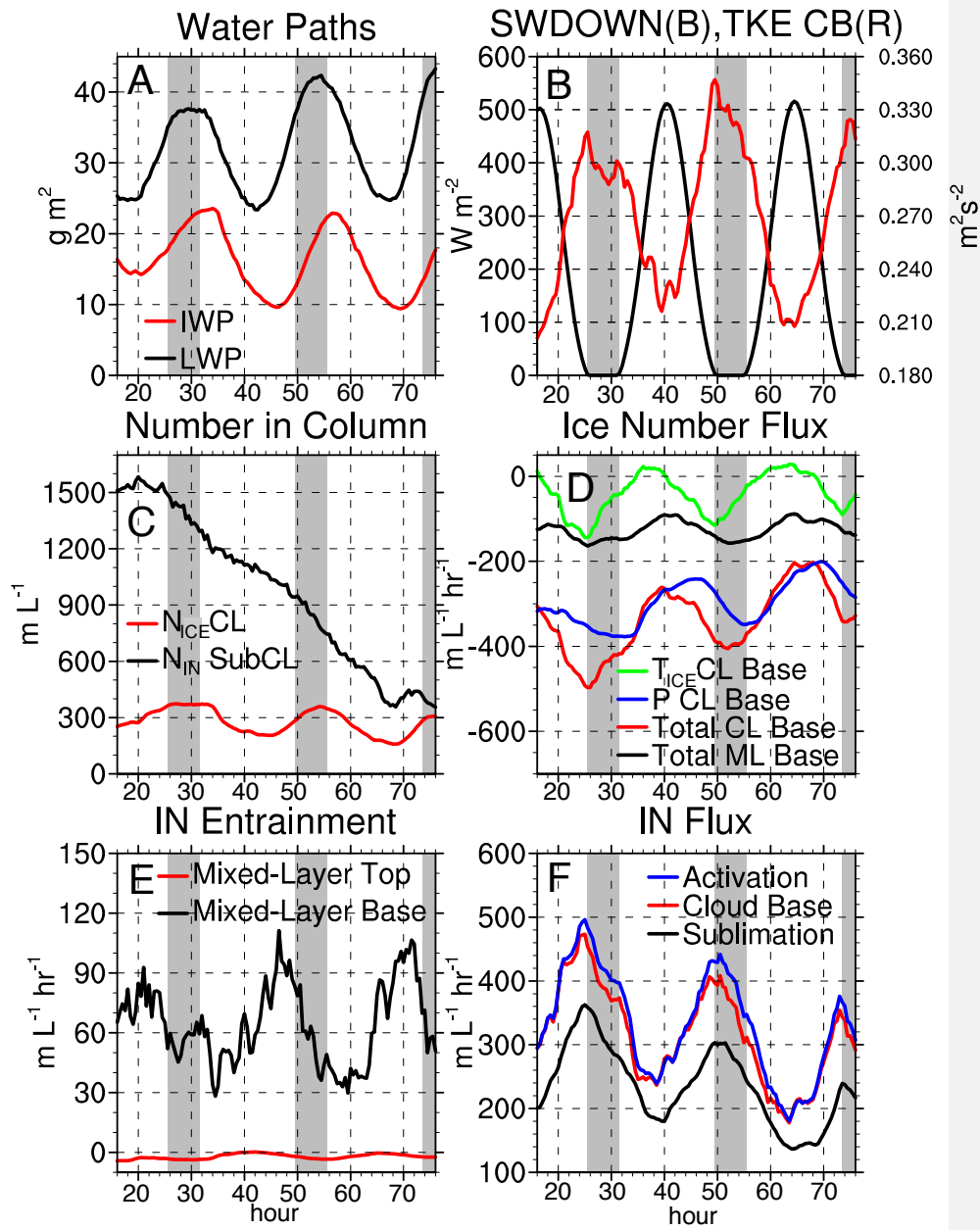
824

825 **Figure 9:** Horizontally-averaged fluxes from Control and NoRecycle integrations for hours
 826 6-40 (smoothed with 90 minute running average). NoRecycle shown with dashed lines. A)
 827 N_{ICE} flux at cloud base due to turbulence+subsidence+precipitation (red), mixed-layer base
 828 due to turbulence+subsidence+precipitation (black), and due to activation (multiplied by -1,
 829 blue), in units of $m L^{-1} hr^{-1}$. B) N_{IN} flux at cloud base (indicated by CB in legend) due to
 830 turbulence (red), N_{IN} flux due to sublimation (black), and precipitation of N_{ICE} at cloud base
 831 (multiplied by -1, blue), in units of $m L^{-1} hr^{-1}$. C) N_{IN} entrainment at mixed-layer top (red)
 832 and base (black), in units of $m L^{-1} hr^{-1}$.



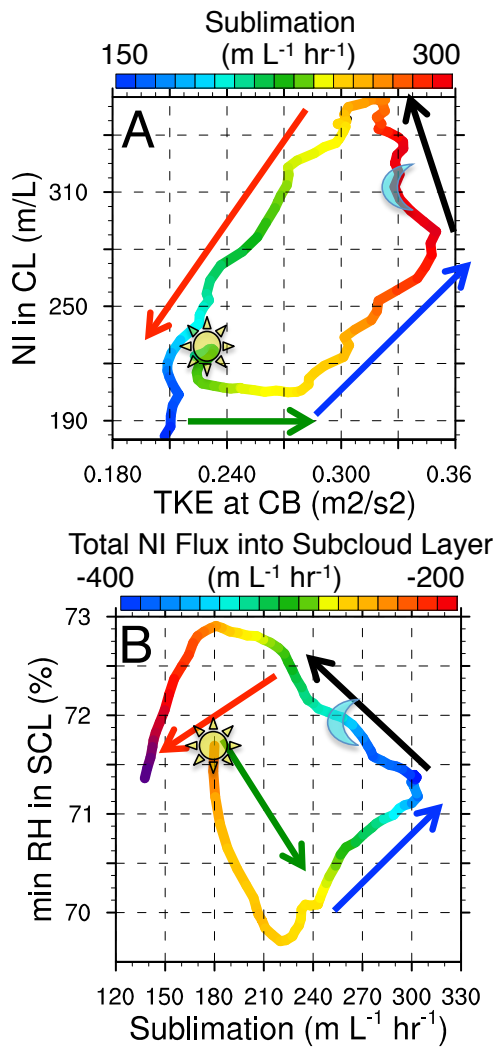
833

834 **Figure 10:** Schematic of feedback loops that maintain ice production and the phase-
 835 partitioning between cloud liquid and ice in AMPS when recycling is allowed. Red colors
 836 denote N_{IN} . Blue colors denote N_{ICE} . Vertical profiles of N_{ICE} , N_{IN} , relative humidity, and
 837 temperature shown with thin blue, red, green, and yellow lines, respectively.



838

839 **Figure 11:** SW time series (see Figure captions).



840

841 **Figure 12:** A) Phase diagram of TKE at cloud base vs. N_{ICE} in the cloud layer starting at
 842 peak shortwave hour 40, in units of $m L^{-1}$ and $m L^{-1} hr^{-1}$, respectively. Colors show
 843 sublimation in units of $m L^{-1} hr^{-1}$. B) 24-hour phase diagrams of sublimation vs. minimum
 844 relative humidity in the subcloud layer starting at peak shortwave hour 40, in units of $m L^{-1}$
 845 hr^{-1} and %, respectively. Colors show total N_{ICE} flux at cloud base, $m L^{-1} hr^{-1}$. Hours 42-47,
 846 47-50, 50-56, and 57-62 indicated with green, blue, black, red arrows, respectively.

847 Minimum shortwave indicated with the moon symbol. Maximum shortwave indicated with
848 the sun symbol.